ELSEVIER

Contents lists available at ScienceDirect

# Chemical Engineering Journal

journal homepage: www.elsevier.com/locate/cej



# Visible-light photodegradation of sulfamethoxazole (SMX) over Ag-P-codoped g-C<sub>3</sub>N<sub>4</sub> (Ag-P@UCN) photocatalyst in water



Thanh-Binh Nguyen<sup>a</sup>, C.P. Huang<sup>b</sup>, Ruey-an Doong<sup>c</sup>, Chiu-Wen Chen<sup>a</sup>, Cheng-Di Dong<sup>a,\*</sup>

- <sup>a</sup> Department of Marine Environmental Engineering, National Kaohsiung University of Science and Technology, Kaohsiung City, Taiwan
- <sup>b</sup> Department of Civil and Environmental Engineering, University of Delaware, Newark 19716, DE, USA
- <sup>c</sup> Department of Biomedical Engineering and Environmental Sciences, National Tsing Hua University, Hsinchu 30013, Taiwan

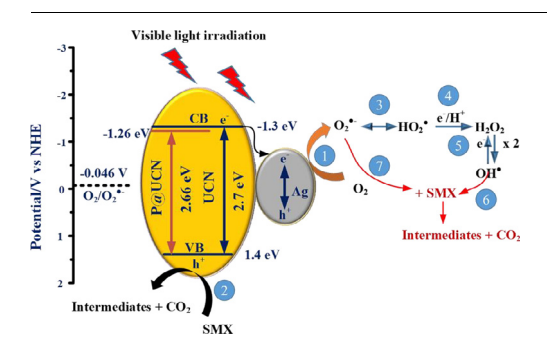
#### HIGHLIGHTS

- A novel Ag-P-doped-g-C<sub>3</sub>N<sub>4</sub> was synthesized for photocatalytic degradation of SMX.
- The visible photoactivity of Ag-Pdoped-g-C<sub>3</sub>N<sub>4</sub> was 7 times as that of g-C<sub>3</sub>N<sub>4</sub>.
- The Ag-P-doped-g-C<sub>3</sub>N<sub>4</sub> was highly recyclable for at least 6 consecutive cycles
- O<sub>2</sub> and OH were responsible for the photodegradation of SMX.
- The photocatalytic mechanism was elucidated.

# ARTICLE INFO

Keywords: Ag-P@g-C<sub>3</sub>N<sub>4</sub> Visible light Photocatalysis Sulfamethoxazole Stability

#### GRAPHICAL ABSTRACT



#### ABSTRACT

Ag-decorated phosphorus doped graphitic carbon nitride (Ag-P@UCN) nanocomposite was successfully synthesized. Ag nanoparticles (average size = 15 nm) were well-crystalline and uniformly dispersed on the P doped g- $C_3N_4$  (P@UCN) surface. Nano-Ag particles enhanced light absorption and acted as electron sink to capture photogenerated electrons, and promoted the separation of photo-induced charge. Results showed greater than 99% of sulfamethoxazole (SMX) removal within 30 min under visible light irradiation. The photodegradation rate of SMX over Ag-P@UCN was  $\sim$ 4 and 7 times faster than that on pristine g- $C_3N_4$  (UCN) and P@UCN, respectively. Ag-P@UCN was stable and could be reused for at least 6 cycles without losing photocatalytic activity. Reactive oxygen species played a significant role in the photodegradation of SMX. Overall, a new scheme to synthesize heterojunction photocatalysts, exemplified by Ag-based nanomaterials, for the heterogeneous photodegradation of organic contaminants under visible light was attained.

# 1. Introduction

Antibiotics, widely used for disease control in humans and animals, are one of the most important products of the pharmaceutical industry. Particularly, sulfamethoxazole (SMX), a sulfonamide antibiotic and one of a broad spectrum of antibiotics, has attracted growing attention in recent years due to its universality, persistence, and potential threats to

aquatic life and human health [1]. The ubiquitous presence of SMX in the natural aquatic environment has been reported [2,3]. Conventional water treatment processes (i.e., coagulation, flocculation, adsorption, biological treatment, and ozonation) have been studied for SMX removal from field and synthetic waste water systems but are not efficient enough to completely degrade SMX [4]. Thus, effective elimination of SMX from surface water is important to protect human health and

E-mail address: cddong@nkust.edu.tw (C.-D. Dong).

<sup>\*</sup> Corresponding author.

ecological safety. Photocatalysis has emerged as a green and efficient alternative to conventional techniques for the removal of emerging contaminants such as antibiotics [5,6].

Graphitic carbon nitride (g-C<sub>3</sub>N<sub>4</sub>), a metal-free visible-light-responsive photocatalyst, has recently attracted great attention for applications in water splitting and environmental remediation by virtue of its low cost, high photostability, bulk-production, and appealing optical properties [7]. Although g-C<sub>3</sub>N<sub>4</sub> photocatalyst has been intensively studied in the past few years, it still suffers from a number of disadvantages, such as low visible-light utilization efficiency, possibility of high charge carrier recombination, and low surface area [8]. After years of effort, different approaches have been advanced to improve the photocatalytic activity of g-C<sub>3</sub>N<sub>4</sub> such as the fabrication of g-C<sub>3</sub>N<sub>4</sub> based heterojunction [9], heteroatom doping [10], and dye sensitization [11]. Recently, phosphorus doping has attracted much attention due to easy preparation and high performance. P doping effectively alters the band structure, improves the separation of charge carriers, decreases the band gap energy and expands the range of light absorption of g-C<sub>3</sub>N<sub>4</sub> [7,12]. However, the application of phosphorus-loaded-thin g-C<sub>3</sub>N<sub>4</sub>, P@ UCN, in photocatalysis is still hampered by low efficiency if lacking further modification. To further improve the photocatalytic performance of P@UCN, doping of noble metal nanoparticles such as Au, Ag, and Pt has been attempted as to enhance the visible light absorption by the localized surface plasmon resonance (LSPR) effect, resulted from the collective oscillation of surface electrons induced by the electromagnetic field of the incident light [13]. Moreover, noble metals can act as photogenerated e - traps, thereby prolonging the lifetime of charge carriers (e<sup>-</sup>/h<sup>+</sup>). Among the noble metals, Ag has attracted the most attention because of excellent stability, antibacterial property, and lower cost [14]. Thus, it is hypothesized that decorating the surface of P@UCN with Ag nanoparticles (Ag NPs) will enhance the photocatalytic performance through increased light absorption, with respect to wavelength and intensity, and efficient separation of photogenerated e<sup>-</sup>/h<sup>+</sup> pairs. To the best of our knowledge, the simultaneous doping of Ag NPs and P onto g-C<sub>3</sub>N<sub>4</sub> nanosheets for enhancing the photocatalytic degradation of SMX has not been reported.

Therefore, the aim of this study was first to prepare P-doped graphitic carbon nitride nanosheets (P@UCN) using a facile pyrolysis method. Then it was to load Ag nanoparticles (Ag NPs) onto the P-doped thin graphitic carbon nitride sheet by chemical reduction of Ag+ in situ for the final preparation of Ag-P@g-C<sub>3</sub>N<sub>4</sub> composite. The composition, morphology, and optical properties of the catalysts were characterized. Photocatalytic performance and stability of the composite were evaluated in terms of SMX degradation under visible light. Additionally, the toxicity of treated solutions was evaluated by the Microtox® acute toxicity test. Major reactive oxygen species (ROS) responsible for SMX degradation were identified by trapping experiments and electron spin resonance (EPR) analysis. Accordingly, a mechanism, together with reaction pathway, was proposed to describe the photocatalytic degradation of SMX.

#### 2. Materials and method

#### 2.1. Materials

Silver nitrate (AgNO $_3$ , 99.9%), sulfamethoxazole (SMX, 99%), phytic acid (C $_6$ H $_1$ 8O $_2$ 4P $_6$ , 50% w/w in H $_2$ O) and sodium borohydride (NaBH $_4$ , > 98%) were purchased from Sigma-Aldrich (St Lewis, MO, USA). Urea (CON $_2$ H $_4$ , 99.5%) was purchased from J. T. Baker (Phillipsburg, NJ, USA). Milli-Q ultrapure water (18.2 Mcm) was used for the preparation of all solutions. All chemicals were used as received without further purification.

# 2.2. Synthesis of $P@g-C_3N_4$

First, 10 g of urea as g-C<sub>3</sub>N<sub>4</sub> precursor and 0.1 mL of phytic acid as P

source were dissolved in 20 mL of deionized water in a beaker under sonication at 20 °C for 30 min, then the mixture was dried in an oven at 60 °C for 12 h. The dried powder was placed in a crucible with a cover semiclosed, calcined in a muffle furnace at 550 °C for 2 h using a heating rate of 10 °C-min $^{-1}$  in air, and cooled naturally to room temperature to form P@g-C $_3N_4$ . Afterward, the P@g-C $_3N_4$ , also denoted as P@UCN, was collected and milled into uniform-sized powder. For comparison, the g-C $_3N_4$  sample was prepared according to the same method above without the addition of phytic acid, and the corresponding calcination product was denoted as UCN. The yield of UCN and P@UCN after pyrolysis was approximate 0.33 and 0.30 g, respectively.

#### 2.3. Synthesis of Ag-P@g-C<sub>3</sub>N<sub>4</sub>

Ag-P@UCN composite was prepared by *in situ* reduction of Ag $^+$  to Ag on the surface of P@UCN using NaBH4 reducing agent. Typically, 100 mg of the as-prepared *meso*-P@UCN was dispersed in 40 mL of deionized water and ultrasonicated for 30 min to obtain a homogeneous dispersion. Then 8.3 mg of AgNO3 aqueous solution (equivalent to 5 wt % Ag) was added to the above suspension and vigorously stirred at room temperature under Ar atmosphere for 30 min. Ten mL of 4.9  $\times$  10  $^{-3}$  mM NaBH4 solution were added dropwise to the suspension while being continuously stirred for another 2 h at 30 °C to convert Ag $^+$  to Ag NPs. The Ag: NaBH4 molar ratio was  $\sim$  1:10 for all synthesis conditions. Finally, the resulting suspension was collected by filtration, rinsed with ethanol and deionized water several times, freeze-dried, and finally stored in a desiccator until use. No trace of Ag ion was detected in the filtrate, which indicated complete impregnation of all Ag ions onto the P@UCN.

#### 2.4. Characterization

The crystal form of the materials was recorded by X-ray diffraction (XRD, Bruker D8 Advance, Billerica, MA, USA) with Ni-filtered Cu Ka radiation ( $\lambda = 1.5406 \,\text{Å}$ ) operated at a generator voltage of 40 kV and an emission current of 40 mA. The X-ray diffraction patterns were recorded in the 20 angle range from 10° to 85° with a step size of 0.05° and a scan rate of 2°-min-1. The surface morphology of the as-synthesized materials was taken with a field emission scanning electron microscope (FESEM, Hitachi SU8010, Tokyo, Japan) at an acceleration electron voltage of 15 kV. All samples were Pt-coated using Ion Sputter ε-1030 (Hitachi, Tokyo, Japan) to increase the conductivity. Transmission electron microscopy (TEM), high-resolution transmission electron microscopy (HRTEM), selected area electron diffraction (SAED), high-angle annular dark field (HAADF), and elemental mapping images were examined by field-emission transmission electron microscopy (FETEM, FEI Tecnai F20 G2 S-WIN, Hitachi, Tokyo, Japan) operated at 120 and 200 kV. The Brunauer-Emmett-Teller (BET) specific surface area, pore volume, and pore size distribution were determined by N₂ adsorption and desorption at −196 °C using a surface area and porosimetry system (ASAP 2020, Micromeritics, Norcross, GA, USA). The thermal stability of all samples was carried out using thermogravimetric analyzer (TGA) (Mettler Toledo TGA/DSC 3 + STAR, Columbus, OH, USA) in the temperature range of 30-1000 °C (10 °Cmin<sup>-1</sup>) under N<sub>2</sub> (40 mL-min<sup>-1</sup>). Fourier transform infrared (FT-IR) spectra were acquired with Nicolet iS10 FT-IR spectrometer (Thermo Scientific, Waltham, MA, USA) at a resolution of 2 cm<sup>-1</sup> using the standard KBr disk method. Diffuse reflectance UV-vis spectra of the powder were obtained by UV-vis spectrometer (Hitachi U-2900, Tokyo, Japan) in the wavelength range of 200-800 nm. The photoluminescence (PL) properties of samples were carried out using fluorospectrometer (Hitachi F7000, Tokyo, Japan) with the excitation wavelength 365 nm. The time-resolved PL spectroscopy was recorded on a FLS 920 spectrometer (Edinburg Instruments, Edinburg, TX, USA) with 345-nm laser as light source. Electrochemical impedance spectroscopy

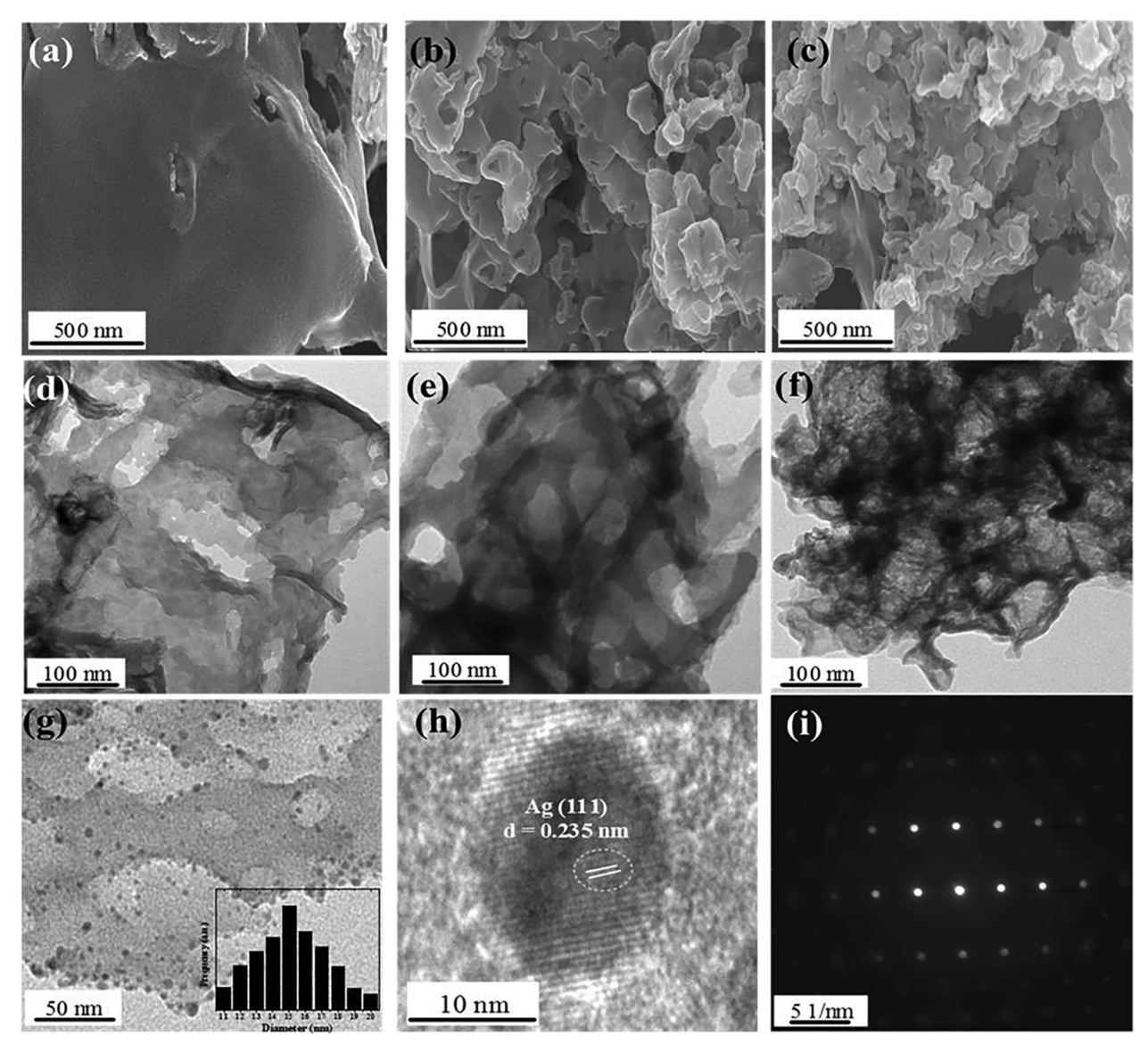


Fig. 1. SEM and TEM images of (a, d) UCN and (b, e) P@UCN; (c) SEM, (f, g) TEM, (h) HRTEM images and (i) SAED pattern of Ag-P@UCN. (Inset of Fig. 1g displayed the size distribution histogram of Ag NPs, suggesting an average size of 15 nm).

(EIS) was performed with an electrochemical work station (Autolab PGSTAT 302 N, Metrolab, Washington DC, USA) in a standard three-electrode configuration at open circuit potential. The sample was coated on a  $1\times 1\,\mathrm{cm^2}$  fluorine tin oxide (FTO) glass electrode at the mass loading of  $0.1\,\mathrm{mg\,cm^{-2}}$ . A Pt wire and Ag/AgCl electrode were used as counter and reference electrodes, respectively. The light source was a 350 W Xenon lamp with a 420 nm cutoff. The electrolyte solution was 0.5 M sodium sulfate (Na<sub>2</sub>SO<sub>4</sub>). Electron paramagnetic resonance (EPR) spectra was recorded on EPR spectrometer (Bruker, EMX-10, Billerica, MA, USA) working at X-band frequency of 9.49–9.88 GHz and power of 8.02 mW. X-ray photoelectron spectroscopy (XPS) measurement was performed on Thermo Escalab 250Xi with Al K $\alpha$  as the excitation source with photon energy of 1486.6 eV. Zeta potential was measured by Zetasizer Nano ZS (Malvern Analytical, Woecestershire, UK) at 25 °C.

#### 2.5. Photodegradation of SMX

SMX photocatalytic degradation experiments and blank runs (i.e., photolysis of SMX without catalyst or with catalysts in dark condition) were conducted using a photoreactor (Rayonet RPR-100, Southern New

England Ultraviolet Co, Branford, CT, USA) equipped with eight 8 W visible lamps ( $\lambda = 465 \pm 40 \, \text{nm}$ ) at room temperature. In each experiment, the as-synthesized photocatalysts suspensions (1000 mgL<sup>-1</sup>) in quartz beaker (100 mL) were dispersed by ultrasonication for 30 min before spiking with SMX stock solution to obtain a final concentration of 5 mg-L<sup>-1</sup>. The initial solution pH was adjusted by 0.1 N of NaOH or HCl. Prior to light irradiation, the mixtures were magnetically stirred in the dark for 60 min to ensure equilibrium adsorption of SMX on the catalyst surface. Subsequently, the photoreactor light source was switched on to begin the photocatalytic reaction. During catalytic experiments, 2 mL aliquots of suspension were drawn from the reaction vessel at a certain time interval and immediately filtered through 0.45-µm polytetrafluoroethylene (PTFE) microporous membranes to collect the supernatant for the analysis of residual SMX concentration using a highperformance liquid chromatography system (HPLC Chromaster, Hitachi, Tokyo, Japan) equipped with a Chromaster 5420 ultraviolet-visible (UV-vis) detector at a wavelength of 270 nm, a separation module including a gradient Chromaster 5160 pump, and an analysis column GL Sciences Inertsil ODS-2 (5 µm particle size, 4.6 internal diameter  $\times$  250 mm length). The mobile phase was consisted of 40/60 (v/v) acetonitrile/deionized water eluted isocratically at a flow rate of

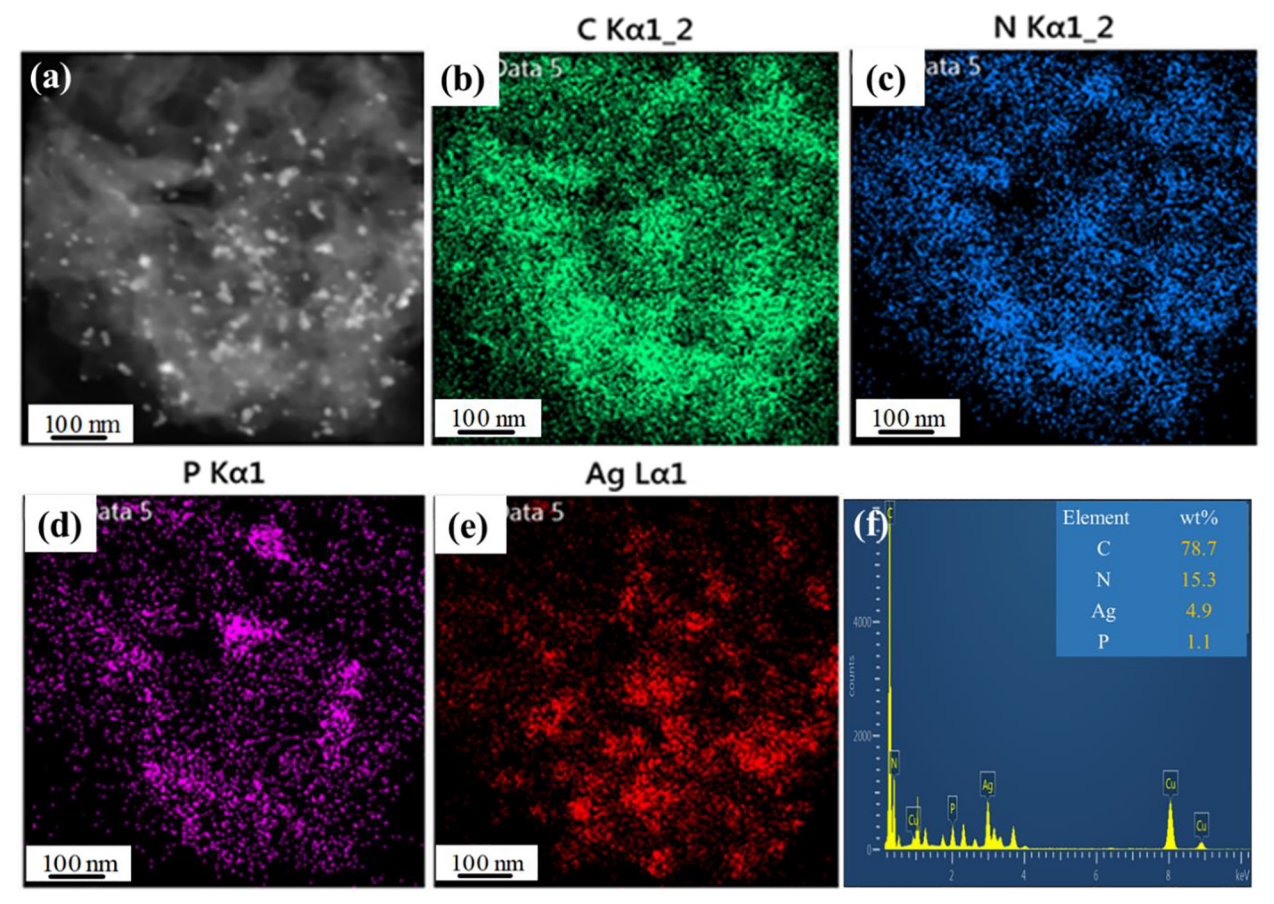


Fig. 2. (a) HADDF-STEM image; (b-e) corresponding elemental mapping of Ag, P, C, N elements; and (f) EDS results of Ag-P@UCN sample.

 $0.8\,mL\,min^{-1};$  the injection volume was  $20\,\mu L$ . The degree of SMX mineralization was evaluated in terms of total organic carbon (TOC) using a Lotix combustion TOC analyzer (Teledyne Tekmar, Mason, OH, USA). All experiments were carried out in triplicate under otherwise identical conditions; all data points were the averages of three independent measurements.

#### 2.6. Microtox® test

Acute toxicity tests were carried out using Microtox Model M500 Toxicity Analyzer (Azur Environmental, Carlsbad, California, USA). V. f ischeri, a luminescent bacteria highly sensitive to toxic compounds, was exposed to the treated solution at 25 °C for 15 min and the luminescence intensity was measured. The inhibition (I) of V. f ischeri was calculated according to Eq. (1), where  $I_{sample}$  and  $I_{blank}$  were the luminescence intensity of the sample solution and the blank solution without SMX.

$$I = \left(1 - \frac{I_{sample}}{I_{blank}}\right) \times 100\% \tag{1}$$

#### 3. Results and discussion

# 3.1. Characterization of photocatalysts

The morphology of the photocatalysts were characterized by SEM and TEM. It can be seen that UCN exhibited lamellar and large stacking sheets (Fig. 1a and d). After P doping, UCN appeared lamellar in irregular stacked sheets, and the sheet size was obviously shrunk compared with UCN (Fig. 1b and e). For Ag-P@UCN nanocomposite, the surface of P@UCN was seen modified with small Ag NPs (Fig. 1c) The TEM

image of Ag-P@UCN revealed small dots with shady color attributed to Ag NPs, which appeared regular shape with diameter in the range of 11-20 nm and were uniformly immobilized on the edges and surface of P@g-C<sub>3</sub>N<sub>4</sub> nanosheets (Fig. 1f, g), which likewise enclosed the complete surface area of the sheet consistently. P@g-C<sub>3</sub>N<sub>4</sub>, which surface was abundant in nitrogen-phosphorus, provided support to improve the dispersibility and control the particle size of Ag nanoparticles. The HRTEM micrograph of Ag-P@UCN showed clear lattice spacing of 0.240 nm, corresponding to the (1 1 1) lattice plane of metallic Ag [14]. The selected area emission diffraction (SAED) pattern of Ag NPs in Ag-P@UCN exhibited dotted concentric rings belonging to the (111), (200), (220) and (311) lattice planes of the Ag face-centered cubic nanocrystalline structure (Fig. 1i) [15]. All of the above observations confirmed the presence of Ag NPs (not agglomerated but well interacted with the interface of P@g-C3N4 sheet), which was expected to facilitate the separation of photogenerated electron-hole pairs and enhance the photocatalytic activity.

The morphology of Ag-P@UCN was further confirmed by high angle annular dark field (HAADF) STEM image (Fig. 2). Likewise, as can be seen from Fig. 2a, the layered and porous P-doped UCN nanosheet with different orientation was fully decorated by bright spots corresponding to tiny Ag NPs, which were active sites that would enhance photocatalytic reaction. Energy-dispersive spectroscopy (EDS) mapping images (Fig. 2b-e) displayed a homogeneous distribution of Ag, P, C, and N elements throughout the composite, which proved successful synthesis of the Ag-P@UCN composite. Furthermore, the weight content of Ag in the composite was 4.9% calculated from the EDS spectrogram (Fig. 2f), which was in good agreement with the amount of Ag used for synthesis.

Fig. 3a presented the XRD patterns of photocatalysts. It can be seen that all samples showed two diffraction peaks at  $2\theta = 13.2$  and  $27.5^{\circ}$ 

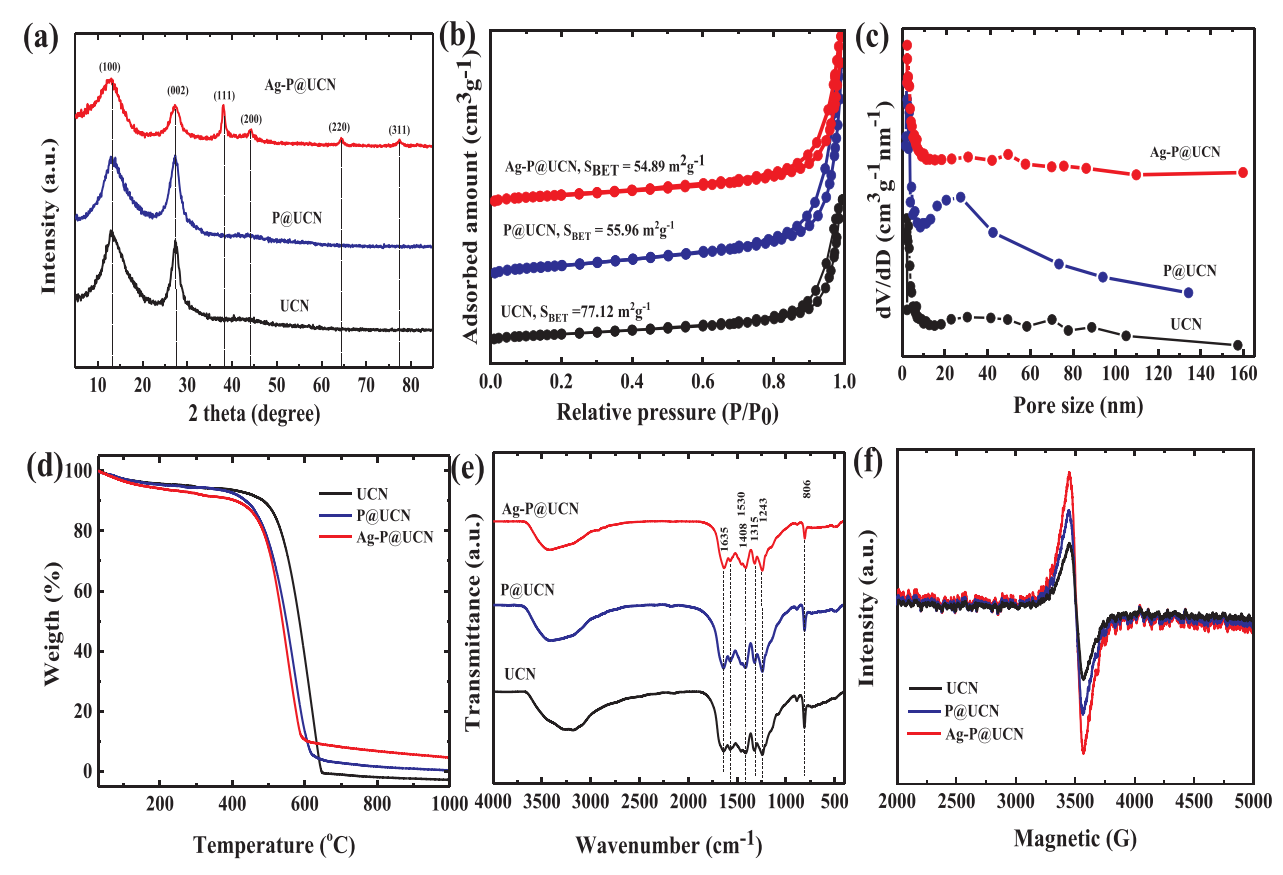


Fig. 3. (a) XRD pattern, (b) Nitrogen adsorption—desorption isotherms, (c) pore size distribution curves, (d) TGA curves, (e) FT-IR spectra and (d) room-temperature EPR spectra of UCN, P@UCN, and Ag-P@UCN.

corresponding to (1 0 0) in-plane structural packing and (0 0 2) plane of interlayer stacking of conjugated aromatic segments, respectively, which confirmed the typical formation of graphitic carbon nitride [16]. Results indicated that the original crystal structure of UCN was retained in both P@UCN and Ag-P@UCN. P@UCN showed a similar XRD pattern as that of UCN, indicating that doping P, at small quantity, did not significantly change the crystal structure of UCN. When P@UCN was decorated with Ag NPs, the intensity of the two diffraction peaks of UCN decreased, which confirmed the highly uniform distribution and dispersion of Ag NPs on the UCN surface. In addition, the characteristic metallic Ag peaks at  $2\theta = 38.3$ , 44.2, 64.3 and 77.3°, easily assigned to the (111), (200), (220) and (311) crystal planes (JCPDS 04-783), respectively, were detected in Ag-P@UCN as well. The average crystallite size (d<sub>hkl</sub>) of Ag NPs was about 15 nm, with respect to the predominant peak along the (111) direction, as calculated by the Scherrer's equation. Result was in good agreement with that of TEM observation.

Fig. 3b and c show the  $N_2$  adsorption-desorption isotherm and the pore size distribution of the as-prepared materials. All samples showed typical type IV isotherm with H3-type hysteresis loop in the relative pressure range of 0.65–0.95, revealing the obvious mesoporous structure nature of g-C<sub>3</sub>N<sub>4</sub> (UNC). The result was in good agreement with that of SEM and TEM observations. In addition, UNC exhibited a broad pore size distribution (2–140 nm) with a two bimodal distribution (i.e., 5 and 55–70 nm) after thermal oxidation process (Fig. 3c), which was attributed to the random-stacking of nanosheets. The adsorption-desorption curve of Au-P@UNC also exhibited type IV isotherm. The specific surface areas of UCN, P@UCN and Ag-P@UCN were 77.12, 55.96, and 54.89 m<sup>2</sup> g<sup>-1</sup>, respectively, which showed reduction of specific surface area of composites after doping with P and Ag NPs. It is noted that the hysteresis loop of Au-P @-gC<sub>3</sub>N<sub>4</sub> shifted slightly to the

relative pressure range of 0.5–0.9, which indicated change of pore texture. Fig. 3c shows the corresponding pore size distribution of photocatalysts measured by BJH method. The pore diameter of P@UCN were 1.8 nm and 24.3 nm, which demonstrated that the micro and mesopores were well developed after the addition of P elements, whereas the bare UCN nanosheets mainly consisted of micropores of approximately 2.4 nm in size. The change in pore size distribution was possibly ascribed to the doping of P which ionic radius was larger than of the replaced C atom that induced local geometrical distortion in the UCN network [17]. Compared with P@UCN, the pore size distribution of Ag-P@UCN mainly centered at 3.2 nm and lower than that of P@UCN, which was due to the embedment of Ag in P@UCN that blocked the large mesopores of P@UCN.

Fig. 3d shows result of thermogravimetric analysis (TGA) of the samples. For the pristine UCN, thermal stability was attained up to 500 °C then weight loss increased dramatically in the range of 500-620 °C, which could be attributed to the sublimation or decomposition of UCN. Compared to UCN, P@UCN showed a lower onset temperature of weight loss (~400 °C), suggesting that P-doping of the UCN network structure weakened the van der Waals forces of the  $\pi$ conjugated system in the UCN structure, which hence facilitated the thermal decomposition of materials to a lesser extent [18]. The amount of P doping in P@UCN, estimated from the residue at the end of TGA in the gas phase, was about 0.97 wt%. For Ag-P@UCN, a similar weight loss pattern with respect to P@UCN was obtained with 5.67 wt% of residual weight fraction. After subtracting the P content from that of the total composite, the empirical composition of Ag amount in the composite was estimated to be ca. 4.6 wt%, which was in good agreement with the result of Ag loading obtained from ICP-OES Analysis.

In order to investigate the molecular structure of the materials, FTIR spectra were recorded (Fig. 3e). All IR absorption bands of the three

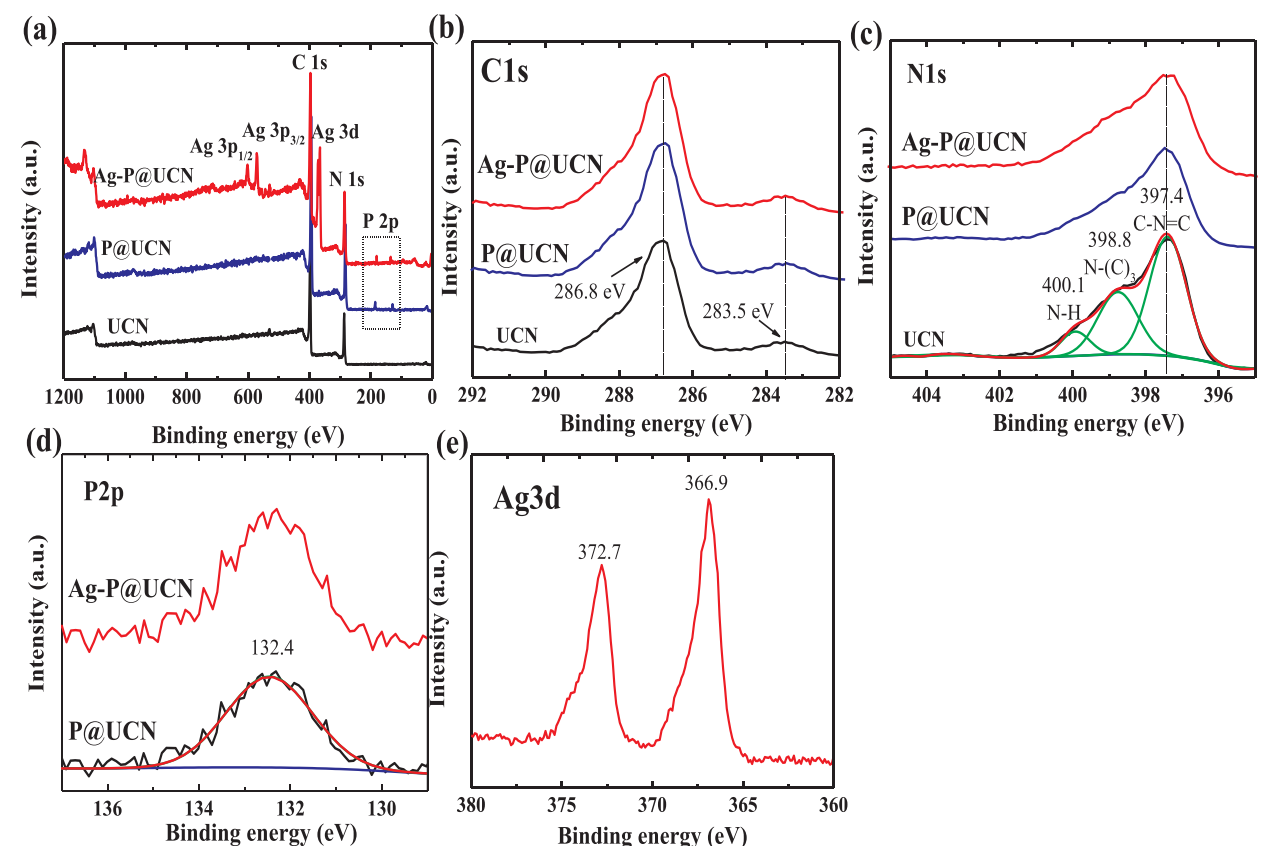


Fig. 4. (a) XPS survey spectra, (b) high resolution XPS spectra of C1s, (c) high resolution XPS spectra of N1s of UCN, P@UCN, and Ag-P@UCN photocatalyst. (d) High resolution P2p XPS spectra of P@UCN and Ag-P@UCN, and (e) high resolution Ag 3d spectra of Ag-P@UCN.

materials were similar, suggesting a stable conjugated structure of the CN skeleton after dopping with P and Ag NPs. A broad absorption band at 3000–3650  ${\rm cm}^{-1}$  was ascribed to the stretching vibration of N–H and O-H moiety of the physically adsorbed water molecule, associated with uncondensed amino groups and surface-adsorbed water molecules [19]. A series of FTIR peaks in the region of 1250-1650 cm<sup>-1</sup> could be assigned to the stretching vibration of aromatic C-N heterocycles in UCN [10]. The FTIR peaks at  $1650-1470 \text{ cm}^{-1}$  were from the aromatic C-N stretching vibration of the heptazine ring, while the peaks at  $1250-14\overline{30}\,\mathrm{cm}^{-1}$  was correspondant to the out-of-plane bending vibrations of the heptazine rings [10]. The FTIR peak at 805 cm<sup>-1</sup> the absorption characteristics of the out-of-plane bending mode of the triazine units [20]. Notably, there were no vibration nor stretching mode of P-related groups, which might be due to low phosphorus content. However, the intensity of peak between 3000 and 3500 cm<sup>-1</sup> significantly decreased with Ag loading, which indicated (i) successful connection of Ag NPs to the CN aromatic rings by coordination bond with N-H and OH moieties as the binding sites, and (ii) coverage and encapsulation of highly dispersed 0-D metallic Ag on the UCN surface that shielded the surface functional groups as demonstrated in TEM results.

It is known that the structure of *meso*-UCN is originated from the formation of *s*-triazine units into an extended  $\pi$ -conjugated system, dependent on the extent of polymerization [21]. Fig. 3f shows the evolution of electronic structure of UCN before and after doping of P and Ag by EPR at room temperature. It can be seen that all three samples showed one single Lorentzian line centering at a G value of 3500, originating from the formation of unpaired electrons on  $\pi$ -conjugated UCN aromatic rings [22]. While pristine UCN nanosheets showed weaker EPR intensity than that of P@UCN and Ag-P@UCN. Results of previous studies showed that P interstitial doping effectively accelerated the electron mobility in the  $\pi$ -conjugated system of *meso*-

UCN and, potentially, due to the electron donation from P species that increased the density state of the conduction band and opened new channels for carrier migration as well as separation [12,17]. After modification with Ag NPs, the EPR intensity was greatly enhanced since Ag NPs would be electron enriched through the simple interface between Ag NPs and P@UCN. The results were clear that Ag-P@UCN would favor the separation and migration of photo-induced charge carriers.

Fig. 4 shows the surface chemical composition and chemical state of elements in the photocatalysts by XPS analysis. The survey scan of UCN, P@CN, and Ag-P@UCN showed clearly that UCN was consisted of mainly C and N elements, while P@UCN exhibited C, N and P elements (Fig. 4a). Further, the peak of Ag element was detected in Ag-P@UCN only. The high resolution XPS spectra of C1s (Fig. 4b) exhibited two peaks at binding energy of 283.5 and 286.8 eV, ascribed to adventitious carbon contamination, and the C-C bond originated from sp2 C atom bonded to the N atoms in the triazine (N<sub>2</sub>–C=N), respectively [16]. The high-resolution N 1s spectra was deconvoluted into three main peaks (Fig. 4c). The peak at 397.4 eV was correspondent to the N with sp<sup>2</sup> hybridized nitrogen (C-N=C) in aromatic triazine rings, whereas the other two peaks at 398.8 and 400.1 eV were ascribed to the ternary nitrogen N-(C)<sub>3</sub> coordination and free N-H functional group [16]. Notably, the slight shift of C1s and N1s peaks in P@UCN and Ag-P@UCN toward lower binding energy side revealed change in electronic structure of the photocatalysts. Fig. 4d gives the high resolution P2p spectra of P@UCN and Ag-P@UCN. The broad peak at 132.4 eV was attributed to P-N coordination, suggesting that P atoms were successfully incorporated into the graphitic C-N network and most probably replaced the C in the triazine rings to form P-N bonds [23]. The Ag 3d fine spectra of Ag-P@UCN showed two distinct peaks at about 366.7 (Ag  $3d_{3/2}$ ) and  $372.7\,\text{eV}$  (Ag  $3d_{5/2}$ ) with a splitting distance of  $6.0\,\text{eV}$ (Fig. 4e), which confirmed the successful loading of metallic Ag species

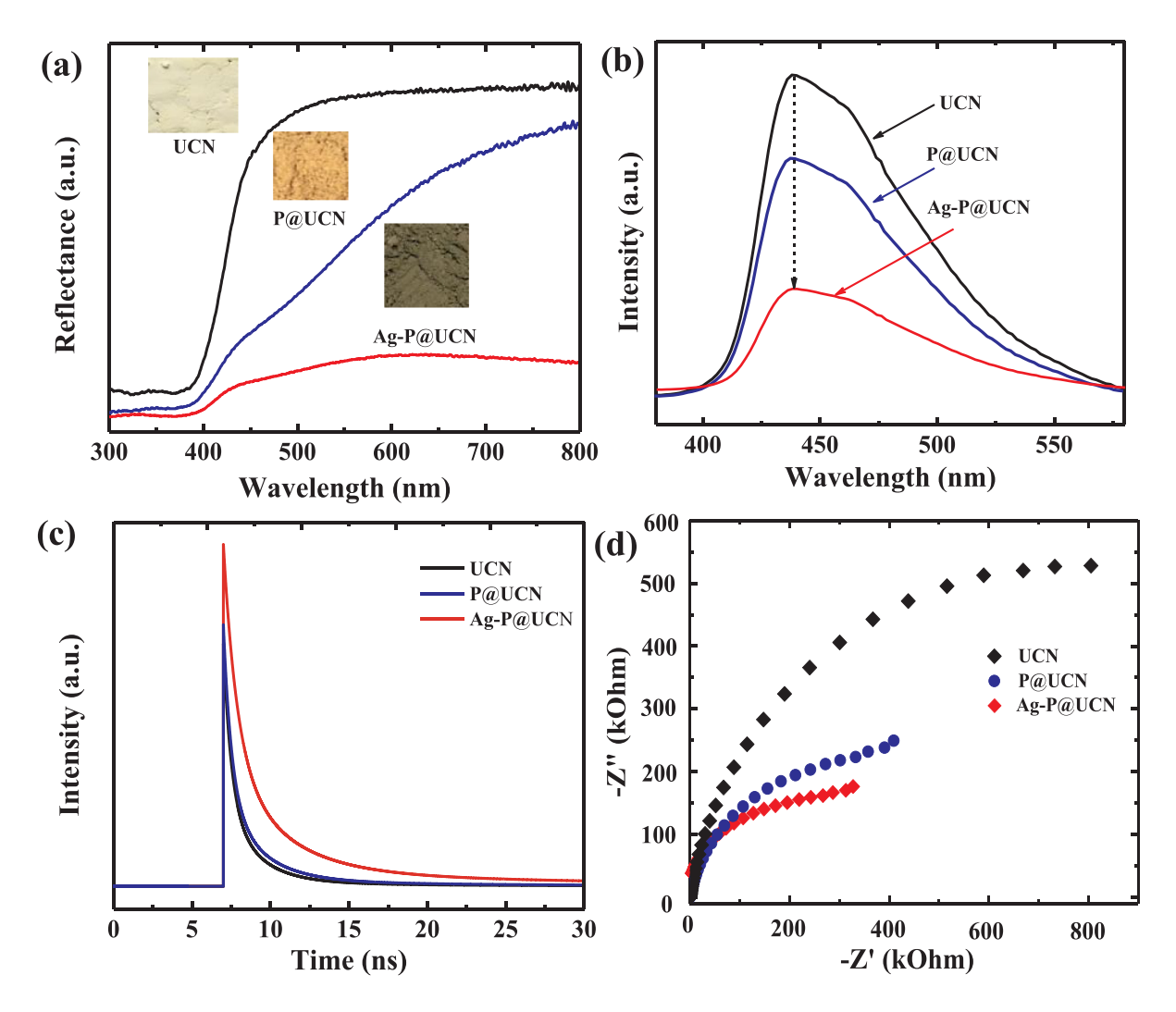


Fig. 5. (a) UV-vis diffuse reflectance spectra, (b) PL spectra, (c) Time-resolved PL spectra, and (d) EIS plot of as-prepared UCN, P@UCN and Ag-P@UCN.

on the P@UCN surface.

The UV-visible diffuse reflectance was used to characterize the optical absorption ability of photocatalysts (Fig. 5a). The original UCN showed the absorption edge in the wavelength range of 450 nm. Compared with the pristine UCN, P@UCN and Ag-P@UCN showed enhanced light absorbance in the range of wavelength longer than 450 nm. The integration of P atoms in the lattice of g-C<sub>3</sub>N<sub>4</sub> extended the visible light response and improved photogenerated charge carriers separation of g-C<sub>3</sub>N<sub>4</sub> due to multiple reflections caused by the porous structure and P-doping function [24]. Further, it can be seen that Ag NPs decorated P@UCN exhibited absorption band in the range of 450-600 nm, which could be attributed to the localized surface plasmon resonance effect of Ag NPs [14]. The lowest reflectance intensity in the visible light range confirmed the promotional role of Ag NPs in trapping excited electrons of P@UCN, preventing more efficient separation of electron-hole pairs, and extending absorption band. The salutary effect of visible light harvesting can also be reflected by macroscopic color changes from canary yellow toward dark brown. In addition, the bandgaps of UCN, P@UCN, and Ag-P@UCN, obtained by Kubelka-Munk method, were 2.7, 2.66, and 2.51 eV, respectively (Fig. S1). Interesting, Chen et al. [25] also reported bandgap of 2.7 and 2.51 eV for P-g-C<sub>3</sub>N<sub>4</sub> and Ag-P-gC<sub>3</sub>N<sub>4</sub>, respectively. Results clearly demonstrated the visible-light photosensitivity on the doping of Ag- and P on UCN.

PL spectra were acquired to analyze the effect of suppressing charge

recombination in UCN, P@UCN, and Ag-P@UCN. As shown in Fig. 5b, pure UCN exhibited a strong emission in the range of 430-500 nm and a maximum intensity at 440 nm, corresponding to the high recombination rate of electron-hole pairs, thus low photocatalytic activity [26]. The PL emission intensity of P@UCN decreased markedly upon the decoration of P heteroatoms. Low PL emission intensity indicated effective separation of photoinduced charges, which might be caused by trapping generated electrons in P defects near the conduction band bottom and thus impeded the recombination of electron-hole pairs. Noteworthy, the dispersion of Ag NPs on the surface of P@UCN led to the lowest PL emission intensity confirming the promotional role of Ag NPs as electron sinks in trapping the photogenerated e<sup>-</sup> from P@UCN and efficiently hampering the direct recombination of electron-hole pairs. Besides, the time-resolved fluorescence decay spectra were further measured (Fig. 5c). The life-time was contributed by three different processes: non-radiative process  $(\tau_1)$ , radiative process  $(\tau_2)$  and energy transfer process  $(\tau_3)$  [27]. Results showed that the average lifetime for Ag-P@UCN was 8.2 ns, which was longer than that of P@UCN (5.4 ns) and UCN (3.1 ns). The greatly prolonged lifetime of charge carriers for Ag-P@UCN, well associated with the high efficient separation of electron-hole pairs, suggested that the Ag-P@UCN structure would benefit photocatalytic reaction.

EIS measurement was carried out to further investigate the charge transfer resistance and the separation efficiency of charge carriers. It was widely accepted that the semicircle diameter in the high frequency

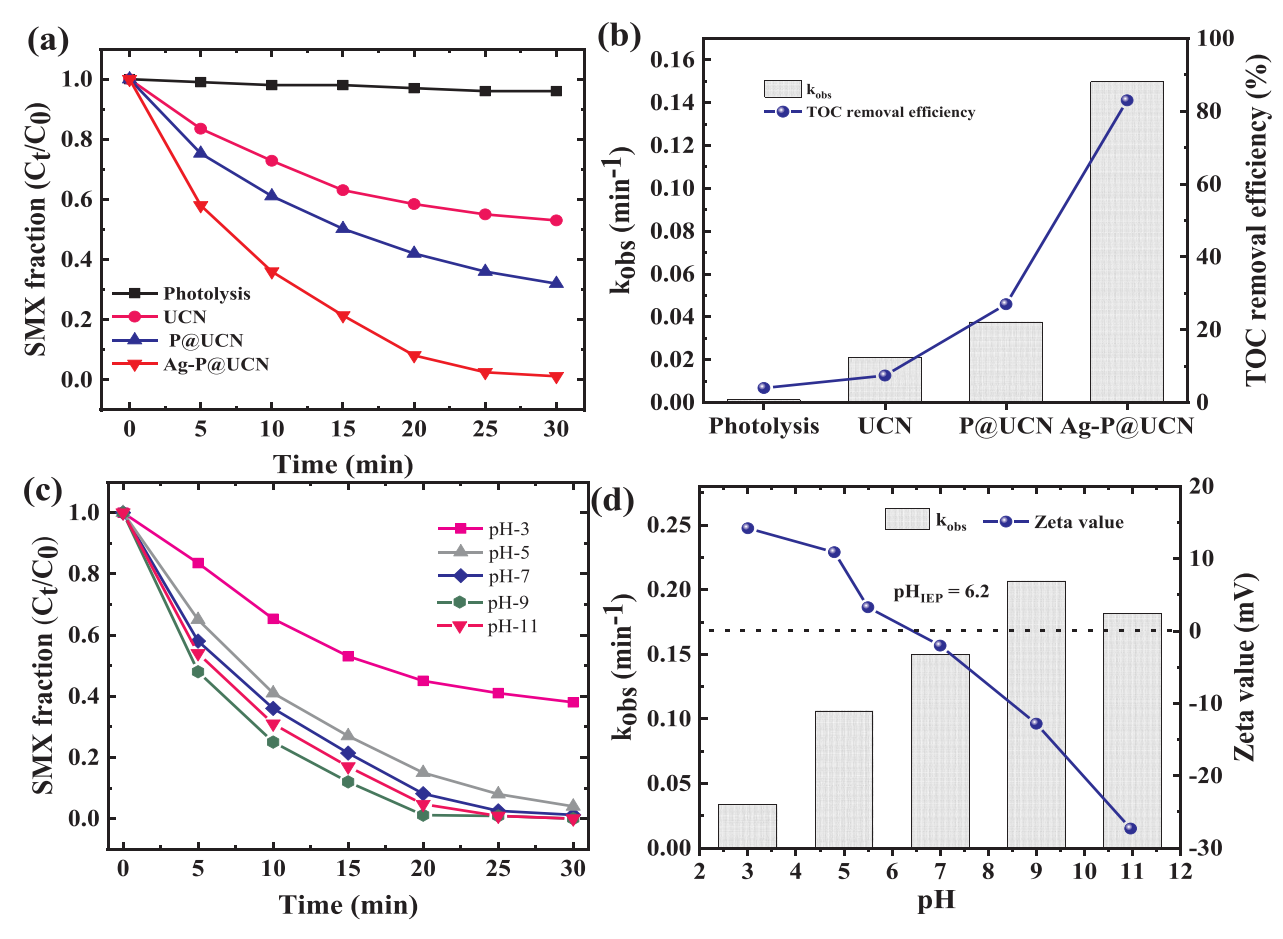


Fig. 6. Effect of different photocatalyst on (a) photodegradation of SMX, and (b) and TOC removal. Effect of initial pH on (c) SMX photodegradation, (d)  $k_{obs}$  and zeta potential of Ag-P@UCN.

region reflected the charge transfer resistance (RCT) between the electrode and the electrolyte [6]. As shown in Fig. 5d, the arc radius (EIS Nyquist plot) of the Ag-P@UCN composite electrode was smaller than those of the P-@UCN and UCN electrodes under visible light irradiation. Results clearly elucidated more effective separation of photogenerated electron-hole pairs and accelerated interfacial charge transfer from Ag-P@UCN composite to reaction molecules than that from UCN or P-UCN.

## 3.2. Photocatalytic performance

The photocatalytic activity of UCN, P@UCN, and Ag-P@UCN composites was studied by the degradation of SMX under visible light irradiation. Fig. 6a shows that the SMX concentration remained unchanged throughout the entire 30 min of visible light irradiation without photocatalyst (direct photolysis). Adsorption experiments were carried out in dark, as to assess the extent of SMX adsorption on UCN, P@UCN and Ag-P@UCN. Results showed that less than 10% of SMX were removed by adsorption (Fig. S2), which indicated that adsorption was not a major process for SMX removal. UCN alone exhibited weak photocatalytic activity toward SMX degradation (47% removal). However, the photocatalytic efficiency was improved to 68% removal over P@UCN. SMX degradation over Ag-P@UCN was drastically enhanced (~99%) compared to other photocatalysts, which was consistent with above results of optical and electrochemical characteristics. Photocatalytic degradation of SMX over the prepared-photocatalysts followed the pseudo-first-order kinetics (Eq. (2)) and the rate constant (kobs) was determined from the slope of linear  $\ln (C_t/C_0)$  vs time (t) plot.

$$ln\left(\frac{C_t}{C_o}\right) = -k_{obs}t\tag{2}$$

where  $C_0$  and  $C_t$  are SMX concentration at initial (t = 0) and time t, respectively. Fig. 6b shows the observed rate constant for different photocatalysts under visible light irradiation. The rate constant followed the order: Ag-P@UCN  $(1.49 \times 10^{-1} \text{ min}^{-1}) > \text{P@UCN}$   $(3.7 \times 10^{-2} \text{ min}^{-1}) > \text{UCN}$   $(2.1 \times 10^{-2} \text{ min}^{-1}) > \text{photolysis}$   $(10^{-3} \text{ min}^{-1})$ . Ag-P@UCN exhibited almost 99% TOC removal after 30 min giving the highest mineralization efficiency, followed by P@UCN and UCN at ~70% and ~48%, respectively. Chen et al. [25] reported a  $k_{\text{obs}}$  of 0.36 min<sup>-1</sup>, which was of the same order of magnitude as obtained in the present study. The above results clearly demonstrated that Ag and P doping synergistically enhanced the photocatalytic activity of UCN under visible light irradiation. Table S1 shows the  $k_{\text{obs}}$  value for SMX photodegradation by different photocatalysts. Results indicated that Ag-P@UCN composite exhibited  $k_{\text{obs}}$  greater than or comparable to most reported data (References in Supplementary data) [33–43]; Ag-P@UCN composite, indeed, was a promising photocatalyst.

The pH can influence SMX degradation because proton affected (i) the generation and distribution of oxidative species and (ii) the interaction between pollutant and catalyst during photodegradation. Results in Fig. 6c showed that after 30 min, there were 98–99% SMX removal at pH 5–11, while only 68% at pH 3. The rate constant increased from  $3.33 \times 10^{-2} \, \mathrm{min^{-1}}$  at pH 3 to  $2.06 \times 10^{-1} \, \mathrm{min^{-1}}$  at pH 9 then slightly dropped to  $1.81 \times 10^{-1} \, \mathrm{min^{-1}}$  at pH 11; following the pH order: 9 > 11 > 7 > 5 > 3 (Fig. 6d). The pH-dependent surface charge of catalysts and the speciation of SMX species impacted the photocatalytic activity of Ag-P@UCN/visible light system. Note that the pH<sub>pzc</sub> of Ag-P@UCN is 6.2 (Fig. 6d) and the pK<sub>a</sub> values of SMX are pK<sub>a1</sub> = 1.6 and

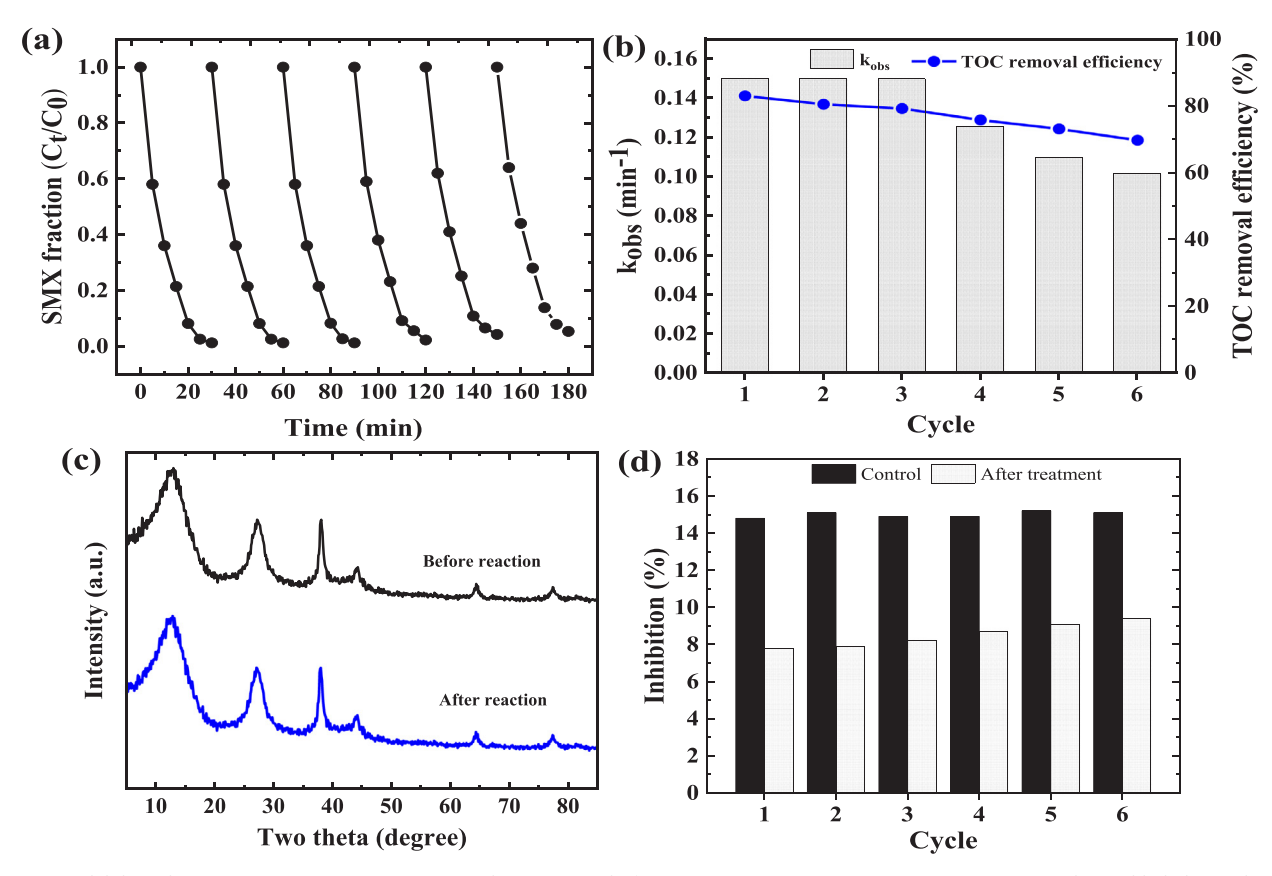


Fig. 7. (a) Recyclability, (b) apparent reaction rate constant and TOC removal of SMX in water over Ag-P@UCN nanocomposite under visible light irradiation. (c) XRD spectra of Ag-P@UNC before and after 6 consecutive cycles. (d) Variation of inhibition to *V. fischeri* toxicity during 6 cycles of SMX degradation.

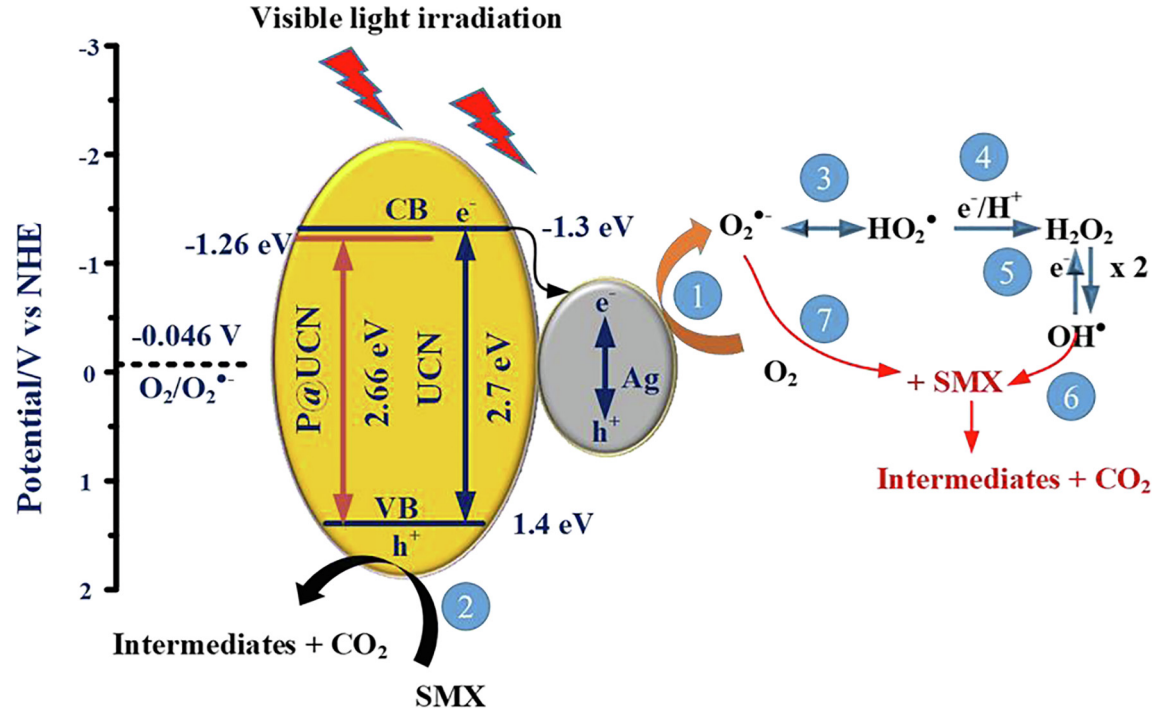


Fig. 8. Schematic illustration of Ag-P@UCN photocatalyst and proposed mechanism of SXM degradation.

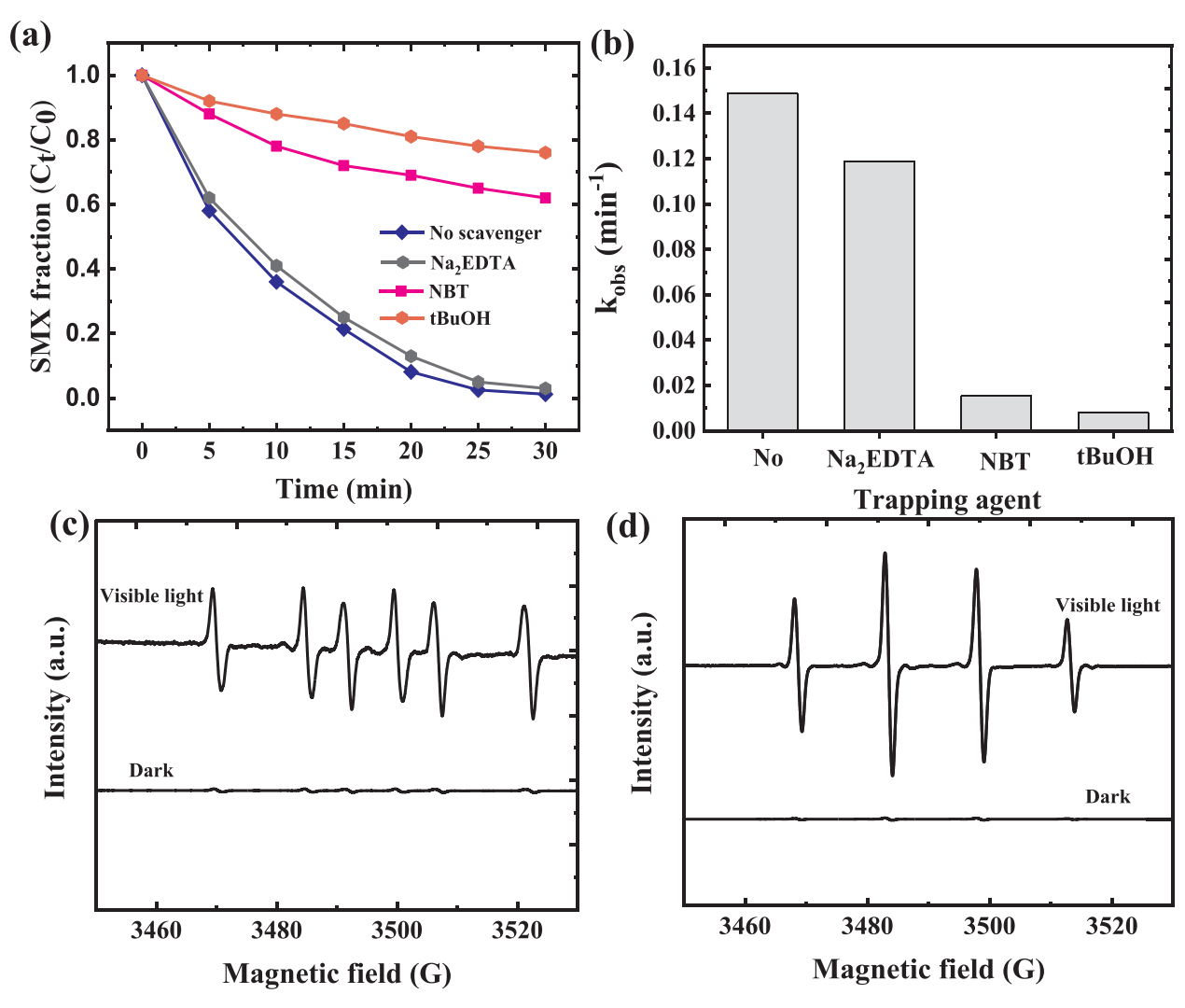


Fig. 9. (a, b) Photocatalytic degradation performance of Ag-P@UCN in SMX removal in the presence of various scavengers, (c) DMPO spin-trapping EPR spectra of  $O_2$  – and (d) DMPO spin-trapping EPR spectra of OH.

 $pK_{a2} = 5.7$  [28], that is, SMX is cationic at pH < 1.6, neutral between pH 1.6 and 5.7, and anionic at pH > 5.7. Therefore, acidic condition (pH 3) did not favored SMX removal by Ag-P@UCN composite. Strong acidic condition limited the adsorption of cationic SMX onto the positively active surface of the catalyst due to strong electrostatic repulsion force. Moreover, Ag NPs was also less stable under acidic condition. which led reduced SMX degradation rate due to loss of Ag [29]. The release of Ag+ ions from Ag-P@UCN at various pH values was also measured via ICP-MS as to assess the stability of Ag NPs. The soluble Ag concentration at solution pH 3 was 25.2 µg L<sup>-1</sup> under visible-light irradiation, but not detectable at pH 5-11. The result evidenced the instability of Ag NPs at acidic pH, which was consistent with the photocatalytic performance of Ag-P@UCN. In general, higher pH favored the photodegradation of SMX, due to formation of deprotonated SMX which was more reactive toward reactive oxygen species than the neutral SMX [30]. However, attack of nucleophilic hydroxyl ions on composite that formed inactive layer covering Ag NPs and repulsion between the anionic SMX and the negatively charged Ag-P@UCN that impeded SMX adsorption were responsible for the slight decrease in rate constant at pH 11.

In order to gain insights into the catalytic activity of Ag-P@UCN toward other types of organic pollutants, degradation experiments were performed by selecting three common dyes used in industry, namely, cationic methylene blue (MB), neutral methyl red (MR) and anionic methyl orange (MO). Under the same reaction conditions, the removal

efficiency was greater than 95%, for all three chemicals, after 30 min of reaction (Fig. S3a). The rate constant and degree of mineralization followed the following decreasing order: MB > MR > MO (Fig. S3b). The results showed that Ag-P@UCN exhibited superior photocatalytic activity toward various organic contaminants under visible light irradiation. Therefore, the visible-light photodegradation of refractory chemicals in water using the Ag-P@UCN composite is promising.

#### 3.3. Stability and recyclability of Ag-P@UCN

The stability and recyclability of photocatalyst are important features for practical applications. Ag-P@UCN exhibited superior photocatalytic activity with rapid and nearly complete photocatalytic degradation of SMX after six photodegradation cycles (Fig. 7a), which clearly demonstrated significantly the stability of Ag-P@UCN photocatalyst. The apparent reaction rate of SMX degradation slightly decreased from  $1.49\times 10^{-1}$  to  $1.01\times 10^{-1}$  min $^{-1}$  at the 6th cycle (Fig. 7b), which may be due to accumulation of intermediates on active surface sites of the photocatalyst [31]. In addition, TOC removal efficiency was largely maintained at in the range of 69.7–83%. The stability of photocatalyst after 6 photocatalytic cycles was also confirmed by the XRD pattern between fresh and spent Ag-P@UCN. Fig. 7c shows no evident crystalline structure change after photocatalysis, indicating excellent stability of the photocatalyst. It must be noted that the soluble silver ion concentrations (detected by ICP-MS) was less than  $5\,\mu g$ -L $^{-1}$ 

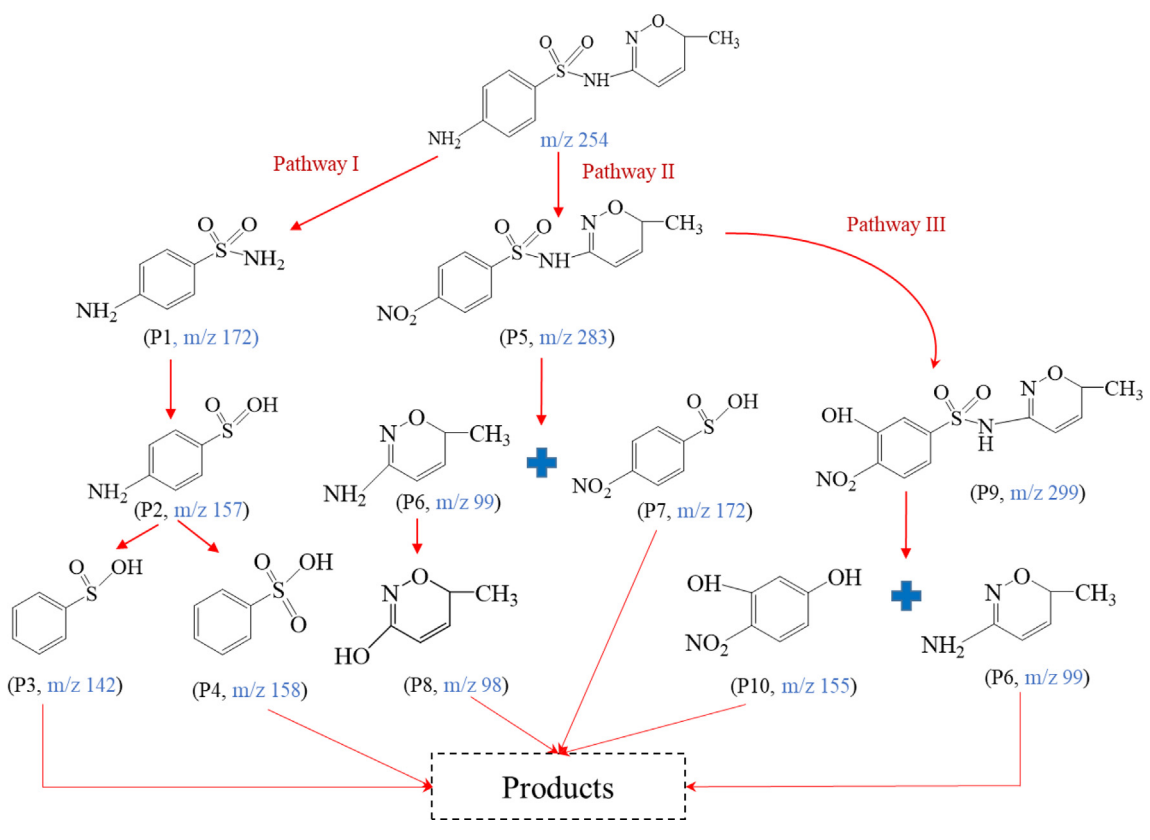


Fig. 10. Proposed SMX degradation pathway in the Ag-P@UNC/visible light system.

after each run.

The SMX treatment efficiency and thus stability of photocatalysts was assessed by evaluating the acute toxicity variation in *V. fischeri* inhibition test by Microtox® for each cycle. As shown in Fig. 7d, the inhibition ratio remained at around 15% for all six control runs using the original SMX solution. The inhibition ratio was decreased to less than 10% at the end of each cycle. Results demonstrated that, after 30 min of treatment with the Ag-P@UCN/visible light system, the toxicity slightly declined, which agreed with results of SMX photodegradation and TOC removal efficiency. Hence, results further confirmed that Ag-P@UCN was highly stable under visible light irradiation for long-term treatment of water containing SMX toward the degradation of hazardous pollutants and toxicity reduction.

#### 3.4. Photocatalytic mechanism

Fig. 8 gives the proposed mechanism of SMX degradation over Ag-P@UCN photocatalyst. It is widely accepted that the valence band (VB) and conduction band (CB) potentials of UCN are, respectively, located at 1.4 and  $-1.3 \, \text{eV}$ , versus normal hydrogen electrode (NHE) [32]. Confirmed by UV-vis reflectance spectra, the band gap of UCN was shortened to 2.66 eV due to P doping, which induced surface-states near the bottom of conduction band of the UCN photocatalyst. The photoexcited e in the CB of P@UCN (-1.26 eV) migrated favorably via the Ag-P@UCN heterojunction (Schottky barrier) to the CB of Ag (+0.8 eV,NHE) due to redox potential difference. The migrated e was effectively stored in Ag after P@UCN excitation, thereby reducing the probability of e<sup>-</sup>-h<sup>+</sup> recombination and enhancing the e<sup>-</sup>-h<sup>+</sup> pair separation in P@UCN. These electrons were subsequently transferred to dissolve oxygen and produced superoxide radicals (Pathway 1). The produced holes also participated in direct oxidation of SMX and generated intermediates and/or CO2 (Pathway 2). However, the redox ability of holes was not strong enough to generate hydroxyl radicals (+2.38 eV vs NHE for OH'/OH"). Nevertheless, hydroxyl radicals might be produced indirectly. The photoexcited  $e^-$  could reduce  $O_2$  to superoxide anion ( $O_2\cdot{}^-$ ) and peroxyl (HO $_2\cdot{}^-$ ) radicals [ $E^0(O_2/O_2\cdot{}^-)=-0.33\,V$  and  $E^0(O_2/HO_2\cdot{}^-)=-0.05\,V$ ] (Pathways 1 and 3). The generated oxygen-containing radicals (HO $_2\cdot{}^-$ ) further reacted through pathways (4 and 5) to produce more powerful ROS, such as highly reactive OH $\cdot$ . At the meantime,  $O_2\cdot{}^-$  and OH $\cdot$  radicals directly participated in the oxidation of SMX and further mineralization of the generated degradation products during the photocatalytic process (Pathways 6 and 7). Chen et al. have also proposed reaction mechanism similar [25].

To further prove the radical degradation mechanism proposed above, radical quenching experiments, using disodium ethylenediaminetetraacetate (Na<sub>2</sub>EDTA), nitroblue tetrazolium (NBT) and, *tert*-butanol (tBuOH) as the scavengers for the hole (h $^+$ ), superoxide anion radical (O<sub>2</sub> $^-$ ), and OH $^\cdot$ , respectively, were performed. Addition of NBT and tBuOH remarkably reduced the degradation of SMX, while the inhibitory effect of Na<sub>2</sub>EDTA was marginal (Fig. 9a and b). The results confirmed that O<sub>2</sub> $^-$  and OH $^\cdot$  were the two primary radicals involved in the degradation process. Furthermore, four characteristic peaks of DMPO - OH $^\cdot$  species in aqueous dispersion and characteristic peaks of DMPO - O2 $^-$  species in methanol dispersion of the catalyst were detected with EPR (Electron Spin Resonance) spectra, which confirmed that O2 $^-$  and OH $^\cdot$  were the main reactive species generated during the photodegradation of SMX by Ag-P@UCN (Fig. 9c and d).

## 3.5. Proposed major SMX degradation pathway

According to the data of TOC removal, the mineralization efficiency of SMX was less than 100%, which indicated incomplete mineralization due to generation of intermediates. Therefore, the reaction intermediates were identified further by LC-QTOF-MS/MS method at the end of reaction (30 min). Fig. S4 shows ion spectra of SMX before and after photodegradation. Results clearly revealed the production of several intermediates. Based on the reaction intermediates identified, a

preliminary reaction pathway was proposed as shown in Fig. 10. Three p degradation pathways were possible for the photodegradation of SMX over Ag-P@UCN. In pathway I, the S - N bond of SMX could be directly attacked by radicals and decomposed to sulfanilamide. (P1). The degradation of intermediate (P1) by radicals resulted in the generation of sulfanilic aicd (P2). Then, sulfanilic acid could lose an amino group or oxygen atom to further decompose into P3 (m/z = 142) and P4 (m/z = 142) z = 158). In pathways II and III, the occurrence of intermediate P5 corresponding to the oxidation of amino group at benzene ring to yield the nitro-SMX derivative. Following pathway II, the breakage of bond between sulfur and benzene ring might result in the generation of products, such as P6 and P7. Furthermore, the hydroxylation effect happened to generate product P8 from P6. In pathway III, oxidation and hydroxylation of nitrogen containing ring of product P5 produced product P9. Afterward, the attack of radicals and bond breaking between S - N of product P9 yielded products P6 and P10. Finally, all small organic fragments were potentially mineralized to carbon dioxide, sulfuric acid, nitric acid, and water.

#### 4. Conclusion

Highly efficient Ag-P@ NP was successfully synthesized by codoping Ag and P on graphitic carbon nitride nanosheets, which reduced the bandgap of UNC significantly from 2.7 to 2.51 eV. Ag-P@UCN photocomposite showed much enhanced visible light photocatalytic activity toward SMX degradation than UCN and P-doped UCN attributable in part to the decrease in hole-electron pair recombination. SMX degradation was pH-dependent with the maximum observed rate constant of  $2 \times 10^{-1} \, \text{min}^{-1}$  at around pH 9.0. The pH-dependent nature of both the speciation of SMX and the surface charge of Ag-P@UNC were factors relating to the controlling effect of pH on the photodegradation of SMX. The photocatalytic stability of Ag-P@UCN was maintained in at least six consecutive cycles without decreasing SMX degradation and crystalline change. Notably, the mineralization of parent SMX compound by the photocatalytic process significantly contributed to the reduction of biotoxicity demonstrated by Mictotox®. The biotoxicity was significantly reduced in the SMX solution treated under visible light irradiation over Ag-P@UNC catalyst. Radical trapping experiment and ESR analysis indicated that  $O_2$ . and OH were the dominant active species responsible for the photodegradation of SMX in the Ag-P@UCN system. Results clearly demonstrated that the Ag-P@UCN composite was a green photocatalyst having high degree of performance under visible-light irradiation for the detoxification of antibiotic compounds, exemplified by SMX. Further study is needed to optimize Ag-P@UCN/ visible light system for practical applications of the present heterogeneous catalytic process. Overall, Ag-P@UCN will be a promising visible-light-sensitive photocatalyst having wide applications in water treatment, solar energy conversion, and other related fields.

# **Declaration of Competing Interest**

The authors declare that they have no known competing financial interests or personal relationships that could have appeared to influence the work reported in this paper.

# Acknowledgments

The authors wish to thank the Ministry of Science and Technology (MOST), Taiwan, for generous financial support under grant No. 106-2221-E-002-002-MY3. Addition support was provided by US NSF IOA (1632899) to CPH.

#### Appendix A. Supplementary data

Supplementary data to this article can be found online at https://doi.org/10.1016/j.cej.2019.123383.

#### References

- [1] A. Mirzaei, L. Yerushalmi, Z. Chen, F. Haghighat, Photocatalytic degradation of sulfamethoxazole by hierarchical magnetic ZnO@g-C<sub>3</sub>N<sub>4</sub>: RSM optimization, kinetic study, reaction pathway and toxicity evaluation, J. Hazard. Mater. 359 (2018) 516–526.
- [2] S. Suzuki, M. Ogo, T. Koike, H. Takada, B. Newman, Sulfonamide and tetracycline resistance genes in total- and culturable-bacterial assemblages in South African aquatic environments, Front. Microbiol. 6 (2015) 8.
- [3] M.B. Kurade, J.Q. Xiong, Govindwar, H.S. Roh, G.D. Saratale, B.H. Jeon, H. Lim, Uptake and biodegradation of emerging contaminant sulfamethoxazole from aqueous phase using Ipomoea aquatica, Chemosphere 225 (2019) 696–704.
- [4] Y.L. Song, J.Y. Tian, S.S. Gao, P.H. Shao, J.Y. Qi, F.Y. Cui, Photodegradation of sulfonamides by g-C<sub>3</sub>N<sub>4</sub> under visible light irradiation: Effectiveness, mechanism and pathways, Appl. Catal. B: Environ. 210 (2017) 88–96.
- [5] T.B. Nguyen, R.A. Doong, Fabrication of highly visible-light-responsive ZnFe<sub>2</sub>O<sub>4</sub>/ TiO<sub>2</sub> heterostructures for the enhanced photocatalytic degradation of organic dyes, Rsc Adv. 6 (2016) 103428–103437.
- [6] T.B. Nguyen, C.P. Huang, R.A. Doong, Photocatalytic degradation of bisphenol A over a ZnFe<sub>2</sub>O<sub>4</sub>/TiO<sub>2</sub> nanocomposite under visible light, Sci. Total Environ. 646 (2019) 745–756
- [7] M. Bellardita, E.I. Garcia-Lopez, G. Marci, I. Krivtsov, J.R. Garcia, L. Palmisano, Selective photocatalytic oxidation of aromatic alcohols in water by using P-doped g-C<sub>3</sub>N<sub>4</sub>, Appl. Catal. B: Environ 220 (2018) 222–233.
- [8] W.D. Oh, V.W.C. Chang, Z.T. Hu, R. Goei, T.T. Lim, Enhancing the catalytic activity of g-C<sub>3</sub>N<sub>4</sub> through Me doping (Me = Cu, Co and Fe) for selective sulfathiazole degradation via redox-based advanced oxidation process, Chem. Eng. J. 323 (2017) 200–260
- [9] W.K. Jo, S. Tonda, Novel CoAl-LDH/g-C<sub>3</sub>N<sub>4</sub>/RGO ternary heterojunction with notable 2D/2D/2D configuration for highly efficient visible-light-induced photocatalytic elimination of dye and antibiotic pollutants, J. Hazard. Mater. 368 (2019) 778–787.
- [10] L.K.B. Paragas, M.D.G. de Luna, R.A. Doong, Rapid removal of sulfamethoxazole from simulated water matrix by visible-light responsive iodine and potassium codoped graphitic carbon nitride photocatalysts, Chemosphere 210 (2018) 1090-1107
- [11] A. Naseri, M. Samadi, A. Pourjavadi, A.Z. Moshfegh, S. Ramakrishna, Graphitic carbon nitride (g-C<sub>3</sub>N<sub>4</sub>)-based photocatalysts for solar hydrogen generation: recent advances and future development directions, J. Mater. Chem. A 5 (2017) 23406–23433.
- [12] L.B. Jiang, X.Z. Yuan, G.M. Zeng, X.H. Chen, Z.B. Wu, J. Liang, J. Zhang, H. Wang, Phosphorus- and Sulfur-Codoped g-C<sub>3</sub>N<sub>4</sub>: Facile Preparation, Mechanism Insight, and Application as Efficient Photocatalyst for Tetracycline and Methyl Orange Degradation under Visible Light Irradiation. ACS Sustain, Chem. Eng. 5 (2017) 5831–5841.
- [13] K.H. Leong, A. Abd Aziz, L.C. Sim, P. Saravanan, M. Jang, D. Bahnemann, Mechanistic insights into plasmonic photocatalysts in utilizing visible light, Beilstein J. Nanotechnol. 9 (2018) 628–648.
- [14] P.C. Nagajyothi, M. Pandurangan, S.V.P. Vattikuti, C.O. Tettey, T.V.M. Sreekanth, J. Shim, Enhanced photocatalytic activity of Ag/g-C<sub>3</sub>N<sub>4</sub> composite, Sep. Purif. Technol. 188 (2017) 228–237.
- [15] K. Jyoti, M. Baunthiyal, A. Singh, Characterization of silver nanoparticles synthesized using Urtica dioica Linn. leaves and their synergistic effects with antibiotics, J. Radiat. Res, Appl. Sci. 9 (2016) 217–227.
- [16] T.B. Nguyen, C.P. Huang, R.A. Doong, Enhanced catalytic reduction of nitrophenols by sodium borohydride over highly recyclable Au@graphitic carbon nitride nanocomposites, Appl. Catal. B: Environ 240 (2019) 337–347.
- [17] X.X. Fang, L.B. Ma, K. Liang, S.J. Zhao, Y.F. Jiang, C. Ling, T. Zhao, T.Y. Cheang, A.W. Xu, The doping of phosphorus atoms into graphitic carbon nitride for highly enhanced photocatalytic hydrogen evolution, J. Mater. Chem. A 7 (2019) 11506–11512.
- [18] W.J. Ong, L.L. Tan, Y.H. Ng, S.T. Yong, S.P. Chai, Graphitic Carbon Nitride (g-C<sub>3</sub>N<sub>4</sub>)-Based Photocatalysts for Artificial Photosynthesis and Environmental Remediation: Are We a Step Closer To Achieving Sustainability? Chem. Rev. 116 (2016) 7159–7329.
- [19] R. Abazari, A.R. Mahjoub, G. Salehi, Preparation of amine functionalized g-C<sub>3</sub>N<sub>4</sub>@(MOF)-M-H/S NCs with visible light photocatalytic characteristic for 4-nitrophenol degradation from aqueous solution, J. Hazard. Mater. 365 (2019) 921–931.
- [20] L. Heymann, S.C. Bittinger, C. Klinke, Molecular Doping of Electrochemically Prepared Triazine-Based Carbon Nitride by 2,4,6-Triaminopyrimidine for Improved Photocatalytic Properties, ACS Omega 3 (2018) 17042–17048.
- [21] X.B. Li, A.F. Masters, T. Maschmeyer, Photocatalytic Hydrogen Evolution from Silica-Templated Polymeric Graphitic Carbon Nitride-Is the Surface Area Important? Chemcatchem 7 (2015) 121–126.
- [22] T.B. Nguyen, R.A. Doong, C.P. Huang, C.W. Chen, C.D. Dong, Activation of persulfate by CoO nanoparticles loaded on 3D mesoporous carbon nitride (CoO@meso-CN) for the degradation of methylene blue (MB), Sci. Total Environ. 675 (2019) 531–541.
- [23] M. Wu, J. Zhang, B.B. He, H.W. Wang, R. Wang, Y.S. Gong, In-situ construction of coral-like porous P-doped g-C<sub>3</sub>N<sub>4</sub> tubes with hybrid 1D/2D architecture and high efficient photocatalytic hydrogen evolution, Appl. Catal. B: Environ. 241 (2019) 159–166.
- [24] S.E. Guo, Y.Q. Tang, Y. Xie, C.G. Tian, Q.M. Feng, W. Zhou, B.J. Jiang, P-doped tubular g-C<sub>3</sub>N<sub>4</sub> with surface carbon defects: Universal synthesis and enhanced

- visible-light photocatalytic hydrogen production, Appl. Catal. B: Environ. 218 (2017) 664–671.
- [25] M. Chen, C.S. Guo, S. Hou, L.L. Wu, J.P. Lv, C.H. Hu, In-situ fabrication of Ag/P/g-C<sub>3</sub>N<sub>4</sub> composite with enhanced photocatalytic activity for sulfamethoxazole degradation, J. Haz. Mat. 366 (2019) 219–228.
- [26] Y. You, S.B. Wang, K. Xiao, T.Y. Ma, Y.H. Zhang, H.W. Huang, g-C<sub>3</sub>N<sub>4</sub>/Bi<sub>4</sub>NbO<sub>8</sub>Cl Heterojunction for Enhanced Photocatalytic Hydrogen Production, ACS Sustain. Chem. Eng. 6 (2018) 16219–16227.
- [27] S.P. Adhikari, Z.D. Hood, V. Chen, K.L. More, K. Senevirathne, A. Lachgar, Visible-light-active g-C<sub>3</sub>N<sub>4</sub>/N-doped Sr<sub>2</sub>Nb<sub>2</sub>O<sub>7</sub> heterojunctions as photocatalysts for the hydrogen evolution reaction, Sustain. Energ. Fuels 2 (2018) 2507–2515.
- [28] H.B. Quesada, A.T.A. Baptista, L.F. Cusioli, D. Seibert, C.D. Bezerra, R. Bergamasco, Surface water pollution by pharmaceuticals and an alternative of removal by lowcost adsorbents, Chemosphere 222 (2019) 766–780.
- [29] J.L. Axson, D.I. Stark, A.L. Bondy, S.S. Capracotta, A.D. Maynard, M.A. Philbert, I.L. Bergin, A.P. Ault, Rapid Kinetics of Size and pH-Dependent Dissolution and Aggregation of Silver Nanoparticles in Simulated Gastric Fluid, J. Phys. Chem. C 119 (2015) 20632–20641.
- [30] S.S. Gao, Z.W. Zhao, Y.P. Xu, J.Y. Tian, H. Qi, W. Lin, F.Y. Cui, Oxidation of sulfamethoxazole (SMX) by chlorine, ozone and permanganate-A comparative study, J. Hazard. Mater. 274 (2014) 258–269.
- [31] T.B. Nguyen, R.A. Doong, Heterostructured ZnFe<sub>2</sub>O<sub>4</sub>/TiO<sub>2</sub> nanocomposites with a highly recyclable visible-light-response for bisphenol A degradation, RSC Adv. 7 (2017) 50006–50016.
- [32] J. Safaei, H. Ullah, N.A. Mohamed, M.F.M. Noh, M.F. Soh, A.A. Tahir, N.A. Ludin, M.A. Ibrahim, W. Isahak, M.A.M. Teridi, Enhanced photoelectrochemical performance of Z-scheme g-C<sub>3</sub>N<sub>4</sub>/BiVO<sub>4</sub> photocatalyst, Appl. Catal. B: Environ. 234 (2018) 296–310.
- [33] A. Kumar, G. Sharma, A.H. Al-Muhtaseb, M. Naushad, A.A. Ghfar, F.J. Stadler, Quaternary magnetic BiOCl/g-C<sub>3</sub>N<sub>4</sub>/Cu<sub>2</sub>O/Fe<sub>3</sub>O<sub>4</sub> nano-junction for visible light and solar powered degradation of sulfamethoxazole from aqueous environment, Chem. Eng. J. 334 (2018) 462–478.

- [34] Y.L. Song, J.Y. Qi, J.Y. Tian, S.S. Gao, F.Y. Cui, Construction of Ag/g-C<sub>3</sub>N<sub>4</sub> photo-catalysts with visible-light photocatalytic activity for sulfamethoxazole degradation, Chem. Eng. J. 341 (2018) 547–555.
- [35] L.F. Chiang, R.A. Doong, Enhanced photocatalytic degradation of sulfamethoxazole by visible-light-sensitive TiO<sub>2</sub> with low Cu addition, Sep. Purif. Technol. 156 (2015) 1003–1010.
- [36] A. Tsiampalis, Z. Frontistis, V. Binas, G. Kiriakidis, D. Mantzavinos, Degradation of Sulfamethoxazole Using Iron-Doped Titania and Simulated Solar Radiation, Catalysts 9 (2019) 16.
- [37] S.K. Ray, D. Dhakal, S.W. Lee, Insight into sulfamethoxazole degradation, mechanism, and pathways by AgBr-BaMoO<sub>4</sub> composite photocatalyst, J. Photochem. Photobiol. A 364 (2018) 686–695.
- [38] E. Ioannidou, Z. Frontistis, M. Antonopoulou, D. Venieri, I. Konstantinou, D.I. Kondarides, D. Mantzavinos, Solar photocatalytic degradation of sulfamethoxazole over tungsten - Modified TiO<sub>2</sub>, Chem. Eng. J. 318 (2017) 143–152.
- [39] E. Borowska, J.F. Gomes, R.C. Martins, R.M. Quinta-Ferreira, H. Horn, M. Gmurek, Solar photocatalytic degradation of sulfamethoxazole by TiO<sub>2</sub> modified with noble metals. Catalysts 9 (2019) 6.
- [40] T. Tomara, Z. Frontistis, A. Petala, D. Mantzavinos, Photocatalytic performance of Ag<sub>2</sub>O towards sulfamethoxazole degradation in environmental samples, J. Environ. Chem. Eng. 7 (2019) 103177.
- [41] A. Mirzaei, Z. Chen, F. Haghighat, L. Yerushalmi, Hierarchical magnetic petal-like Fe<sub>3</sub>O<sub>4</sub>-ZnO@g-C<sub>3</sub>N<sub>4</sub> for removal of sulfamethoxazole, suppression of photocorrosion, by-products identification and toxicity assessment, Chemosphere 205 (2018) 463–474.
- [42] L. Zhou, W. Zhang, L. Chen, H.P. Deng, Z-scheme mechanism of photogenerated carriers for hybrid photocatalyst Ag<sub>3</sub>PO<sub>4</sub>/g-C<sub>3</sub>N<sub>4</sub> in degradation of sulfamethoxazole, J. Colloid Interface Sci. 487 (2017) 410–417.
- [43] F. Beheshti, R.M.A. Tehrani, A. Khadir, Sulfamethoxazole removal by photocatalytic degradation utilizing TiO<sub>2</sub> and WO<sub>3</sub> nanoparticles as catalysts: analysis of various operational parameters, Int. J. Environ. Sci. Technol. 16 (2019) 1–10.